Title: Hydrophilic amorphous crosslinked membranes with subnanometer pores prepared by plasma-enhanced chemical vapor deposition and their shape-selective alcohol permeation

Authors:
Sadaki Samitsu[a]
Email: samitsu.sadaki@nims.go.jp

Edhuan Ismail[b]
Email: binismail.edhuan@nims.go.jp

Yoshihisa Fujii[c]
Email: fujii@chem.mie-u.ac.jp

Izumi Ichinose[b]
Email: ichinose.izumi@nims.go.jp

Affiliations:
[a] Data-driven Polymer Design Group, Research Center for Macromolecules and Biomaterials, National Institute for Materials Science, 1−2−1 Sengen, Tsukuba 305−0047, Japan

[b] Research Center for Macromolecules and Biomaterials, National Institute for Materials Science, 1−1 Namiki, Tsukuba 305−0044, Japan

[c] Department of Chemistry for Materials, Graduate School of Engineering, Mie University, 1577 Kurimamachiya, Tsu, Mie 514-8507, Japan

Corresponding author:
Sadaki Samitsu – *Data-driven Polymer Design Group, Research Center for Macromolecules and Biomaterials, National Institute for Materials Science, 1−2−1 Sengen, Tsukuba 305−0047, Japan;* orcid.org/0000-0002-4139-1656; Email: samitsu.sadaki@nims.go.jp

Hydrophilic amorphous crosslinked membranes with subnanometer pores prepared by plasma-enhanced chemical vapor deposition and their shape-selective alcohol permeation

Sadaki Samitsu,[a]* Edhuan Ismail,[b] Yoshihisa Fujii,[c] Izumi Ichinose [b]

[a] Data-driven Polymer Design Group, Research Center for Macromolecules and Biomaterials, National Institute for Materials Science, 1−2−1 Sengen, Tsukuba 305−0047, Japan
[b] Research Center for Macromolecules and Biomaterials, National Institute for Materials Science, 1−1 Namiki, Tsukuba 305−0044, Japan
[c] Department of Chemistry for Materials, Graduate School of Engineering, Mie University, 1577 Kurimamachiya, Tsu, Mie 514-8507, Japan

Abstract

High-density crosslinked polymer membranes several tens of nanometers thick were prepared by chemical vapor deposition (CVD) of propylamine (PA). Analysis by various methods showed that the densely crosslinked PA-CVD membranes had a composition of $C_{3.0}H_{4.7}N_{0.8}O_{0.4}$, and contained amine, imine, vinyl, and carbonyl functional groups. Positron annihilation lifetime spectroscopy and alcohol-retention studies showed that the crosslinked membranes had pore sizes of 0.3–0.7 nm. Their porosity was about 10%, as estimated from water-absorption experiments. By appropriate choice deposition conditions, the average pore diameter could be selected, and the porosity could be tuned in the range 1–18%. A membrane with 0.56 nm pores showed a significant difference in the retention factors of C3 and C4 alcohols, for example, showing a 77% retention of *tert*-butanol, three times that of *n*-butanol. The thickness of PA-CVD membranes could be reduced to 10 nm, and the membrane showed a high retention performance for divalent ions, a resistance to pressures of more than 40 bars, and a water flux of up to 170 L m^{-2} h^{-1}. This comprehensive investigation of the effects of the CVD parameters will permit tuning of the thickness, pore size, porosity, and density of the hydrophilic crosslinked membranes.

Keywords: PECVD; crosslinked membrane; nanofiltration; shape selective permeation; pore size control

1. Introduction

Ultrathin separation membranes with penetrating subnanometer pores have been widely used in seawater desalination, food processing, pharmaceutical production, and many other applications [1-3]. Crosslinked membranes made of polyamides or polyimides are considered to be the primary materials for separation functional layers [4-7] although carbon materials [8-16], functionalized polyamides [17-19], supramolecular assemblies of fluorine compounds [20, 21], biopolymers [22-25], and porous inorganic materials [26, 27] have all recently received attention as materials for separation layers. Carbon membranes fabricated by means of plasma-enhanced chemical vapor deposition (PECVD) have also been used as nanoporous separation membranes with good mechanical properties [28-30]. Their excellent chemical resistance has attracted considerable attention from the chemical industries.

Porous PECVD membranes can be made from various volatile organic molecules as precursor gases. Their separation performance can be controlled by a suitable choice of membrane-deposition parameters. However, the detailed chemical structures that form the nanometer or subnanometer pores remain unclear.

In the 1970s, pioneering researchers, such as the groups of Buck [31], Hollahan [32], and Yasuda [33], reported on the reverse-osmosis performance of PECVD membranes. Karan et al. [34] reported a high-performance nanofiltration membrane made of diamond-like carbon. Endo and co-workers reported rapid water transport through subnanometer pores in PECVD membranes and they evaluated the pore-size distribution from H_2 adsorption isotherms [35-37]. Silica-based or silicon nitride-based PECVD membranes have been widely studied as gas-separation membranes [38-41].

We previously reported that PECVD membranes made from acetylene or pyridine had elastic moduli of more than 100 GPa, an order of magnitude greater than the strength of hard engineering plastics. These membranes were thought to contain subnanometer pores in the gaps between carbon clusters [34]. On the other hand, PECVD membranes made from N-vinylpyrrolidone or acrylate monomers are generally known as ‘plasma-polymerized membranes’ [42-44]. By using such monomers, it is possible to prepare soft crosslinked membranes with elastic moduli of about 10 MPa [45, 46]. PECVD membranes have hardness values that differ by 10^4 to 10^5 orders of magnitude; that is, their structures range from densely crosslinked diamond-like carbon membranes to loosely crosslinked rubber-like polymer membranes. The size of their subnanometer pores might be controllable by tuning the crosslinking densities of the molecular fragments through the choice of suitable precursors and appropriate manufacturing conditions.

The advantages of the PECVD method are, first, it does not require any specific reactive group in the precursor molecule and, secondly, a variety of organic molecules can be used. In fact, a range of volatile hydrocarbons containing nitrogen, silicon, fluorine, sulfur, or other heteroatoms can be used as precursor gases [47-53]. The vacuum-deposition process permits precise control of the thickness of membranes and permits the fabrication of uniform ultrathin membranes, less than 10 nm thick. Furthermore, multilayer membrane structures can be fabricated by repeating the CVD process with different precursors and/or by changing the deposition parameters. If the size of the nanopores could be controlled by an appropriate selection of the CVD conditions, high-performance membranes with pore-size gradients might be obtained.

The roll-to-roll PECVD method has been used industrially. It will be applied for the rapid and continuous fabrication of separation membranes scalable up to the areas of several hundreds of square meters. We have previously shown that PECVD of organic amines provides hydrophilic membranes that are permeable to molecules of water or various alcohols [34]. The subnanometer pores that penetrated the membrane had porosities of up to 10%. In the present study, we prepared PECVD membranes with elastic moduli of several gigapascals by using propylamine as a precursor gas, and we made a detailed study of the effects of a range of deposition parameters on the separation performance of the resulting membranes. As a result, we found that the size of subnanometer pores in amorphous crosslinked membranes can be precisely controlled, leading to high levels of discrimination between alcohol isomers.

2. Experimental

2.1 Materials and methods

Hydrophilic propylamine (PA) membranes were prepared by the PECVD deposition method using propylamine ($PrNH_2$, Sigma Aldrich, ≥99%) as the precursor gas. Our PECVD system consisted of a 13.5 MHz radio-frequency (RF) power source, mass-flow controllers, a Baratron pressure gauge, a throttle valve, a turbomolecular pump, and parallel-plate electrodes of diameter 60 and 65 mm. The configuration of the system and detailed information pertaining to it are shown in Fig. S1 and Table S1, respectively, of the Supplementary Information (SI).

Glass substrates were used to prepare membrane samples for confocal microscopy, whereas silicon substrates were used to prepare samples for analysis by Fourier-transform infrared spectroscopy (FTIR), atomic force microscopy (AFM), ^{13}C nuclear magnetic resonance (^{13}C NMR) spectroscopy, magic-angle spinning NMR (MAS-NMR), elemental analysis (EA), nanoindentation analysis, ellipsometry, and positron annihilation lifetime spectroscopy (PALS). For the NMR and EA analyses, thick propylamine-CVD (PA-CVD) membranes were initially prepared; these were then removed from the silicon substrate by treatment with aqueous hydrofluoric acid and converted into powder samples. Free-standing samples of PA-CVD membranes were also transferred onto porous alumina substrates for the examination of their cross-sections by scanning electron microscopy (SEM) (SI; Fig. S5).

2.2 Structural characterization

The thicknesses of the PA-CVD membranes were estimated from the difference in height between deposited and nondeposited areas determined by using a confocal microscope (OPTELICS HYBRID; Lasertec Corp., Yokohama) with a white-light interferometer attachment. AFM images were obtained with an SPI-400 instrument (Seiko Instruments Inc., Chiba) operated in the tapping mode. For the thickness measurement, a straight-line was drawn on Si wafer using a marker pen and PA-CVD membrane was deposited. This line acts as a removable mask. After deposition, a razor blade was used to cut the mask along the line. Upon immersing in ethanol, the mask was dissolved and the height difference at the edge of the mask area was measured by confocal laser microscopy. CP/MAS and DD/MAS ^{13}C NMR spectra were obtained by using CMX300 instrument (Chemagnetics, Inc., Fort Collins, CO). FTIR spectra of 2-μm-thick PA-CVD membranes were recorded in the attenuated total reflection mode (ZnSe crystal) by using a FT/IR-6200 instrument (JASCO Corp., Tokyo). We measured the static water contact angle by using a DM-300 instrument (Kyowa Interface Science Co., Ltd., Niiza). High-resolution images of the PA-CVD membranes were recorded by using a field-emission scanning electron microscope (JEM-2100F, JEOL) at an acceleration voltage of 200 kV. Elemental analyses (C, H, N, and O) of PA-CVD membranes were performed by the combustion method using 100−200 mg powder samples.

The hardness and elasticity of the PA-CVD membranes in both dry and wet states were measured by using a Hysitron TriboIndenter (Bruker Corp., Billerica, MS) equipped with a triangular pyramidal Berkovich indenter. The dry samples consisted of 500-nm-thick membranes on Si substrates (50 mm in diameter). The wet samples were prepared by immersing the dry samples in distilled water for 30 minutes.

Water swelling of PA-CVD membranes was assessed by using a high-speed spectroscopic ellipsometer (M-2000U; J. A. Woollam Co., Inc., Lincoln, NE) equipped with a liquid cell. The specimens used were 100- to 300-nm-thick PA-CVD membranes deposited on silicon substrates. The light incident angle was 75° and the wavelength range was 400–1000 nm. We corrected for the phase shift caused by the glass liquid cell by using the value for thermally oxidized silicon (thickness: 259 nm). The rate of deposition of the PA-CVD membrane was also evaluated by using the same ellipsometer in air. First, spectra were obtained by stepwise changes in the incident angle in 5° increments from 55° to 75°. Then, the thickness and the complex refractive index were calculated by simultaneous fitting of the resulting five spectra by using the Cauchy equation ($n = A_n + B_n/\lambda^2 + C_n/\lambda^4$), assuming a three-layer model consisting of the PA-CVD membrane, the natural oxide layer (supposing a certain thickness and parameters), and the silicon substrate [54].

The size distribution of the subnanometer pores was evaluated by pulse-beam positron annihilation lifetime spectroscopy (PALS; PALS-200A; Fuji Imvac Inc.) of 100- to 200-nm-thick PA-CVD membranes on silicon substrates as samples. The chamber pressure was less than 2.5×10^{-9} Torr, the acceleration voltage was 1.0 keV, and the positron count number was integrated up to 5 million counts. The resulting lifetime curves were corrected by using data for the Kapton film and Si substrate measured under the same conditions, and fitted by three components using *PALS-fit* analysis software (Technical University of Denmark, Lyngby). Here, the first-lifetime component was fixed at 0.125 ns, and the average pore radius, d_3, was calculated from the third-lifetime component, τ_3, based on a semiempirical equation [55-57].

2.3 Deposition on porous substrates

To evaluate the coverage of nanometer pores, PA-CVD membranes were deposited on porous alumina supports (pore size 20 nm or 200 nm; Whatman Laboratory Products). After the deposition of a 1.5-nm-thick overlayer of Pt by using a magnetron ion sputter (E-1030; Hitachi), the surface of the sample was examined by FE-SEM (S-4800, Hitachi) at an acceleration voltage of 5 kV and an electron-gun current of 10 μA. The coverage of nanopores was analyzed by extracting the equivalent circles using image-processing software. Then we applied a Gaussian fitting to the pore-size distribution and calculated the average pore diameter, d_{av}, and the deviation, σ.

For the evaluation of permeability, PA-CVD membranes were deposited on asymmetric porous substrates prepared by the non-solvent-induced phase-separation method. The asymmetric substrates were prepared by casting from a 20 wt% solution of poly(phenylsulfone) (PPSU) (Radel R-5000; Solvay Specialty Polymers, Brussels) in N-methylpyrrolidin-2-one (NMP) onto a nonwoven polyolefin sheet and immersing the sheet in water. The surface and cross-section of the asymmetrical substrate were examined by FE-SEM (SU-8200; Hitachi). Pore size of the PPSU substrate was determined to be less than 20 nm. This was also confirmed from the molecular weight cut-off of dextran solutions.

2.4 Separation properties

The separation of alcohols and salts, and the permeability of the membranes to water were evaluated at room temperature by using a dead-end pressure-driven filtration setup with stirring [Fig. S2 (a, b)]. The retention factors of alcohols (1 wt% aqueous solution in total concentration) were evaluated by gas chromatography (GC-2014; Shimadzu) with a flame-ionization detector. Salt-retention factors were evaluated by using 0.2 wt% aqueous solutions of $MgCl_2$ or NaCl containing dilute vitamin B_{12} (1.0 mmol L^{-1}) as a defect indicator. Less than 10% of the feed solution was collected for the evaluation of retention performance. The retention factor, R, was calculated from the concentration difference between the feed and permeate using the following equation:

$$R = (1 - C_p / C_f) \times 100$$

, where C_f and C_p are the concentrations of feed and permeate, respectively. The membrane area was 200 mm^2 and the applied pressure was 2.0 or 4.0 MPa. The permeance, normalized to filtration pressure, J (L m^{-2} h^{-1} bar^{-1}), was calculated by using the following equation:

$$J = V / (A \times T_f \times P_f)$$

, where V (L) is the volume of the filtrate, A (m^2) is the surface area, T_f (h) is the filtration time, and P_f (bar) is the applied pressure. The salt concentration was measured at 20 °C by using a high-precision refractometer (RA-620, Kyoto Electronics). The refractive indices of pure water, aqueous $MgCl_2$ solution, and aqueous NaCl solution are 1.33299, 1.33353, and 1.33339, respectively, and the accuracy of the refractometer was ±0.00001. We have also confirmed the long-term stability of the membrane by filtration experiment of $MgCl_2$ solution up to five days. Nearly 100% of $MgCl_2$ was rejected even after 118 hours although the permeance increased from 0.4 to 0.8 L m^{-2} h^{-1} bar^{-1} [Fig. S2 (c)].

3. Results and discussion

3.1 Membrane production

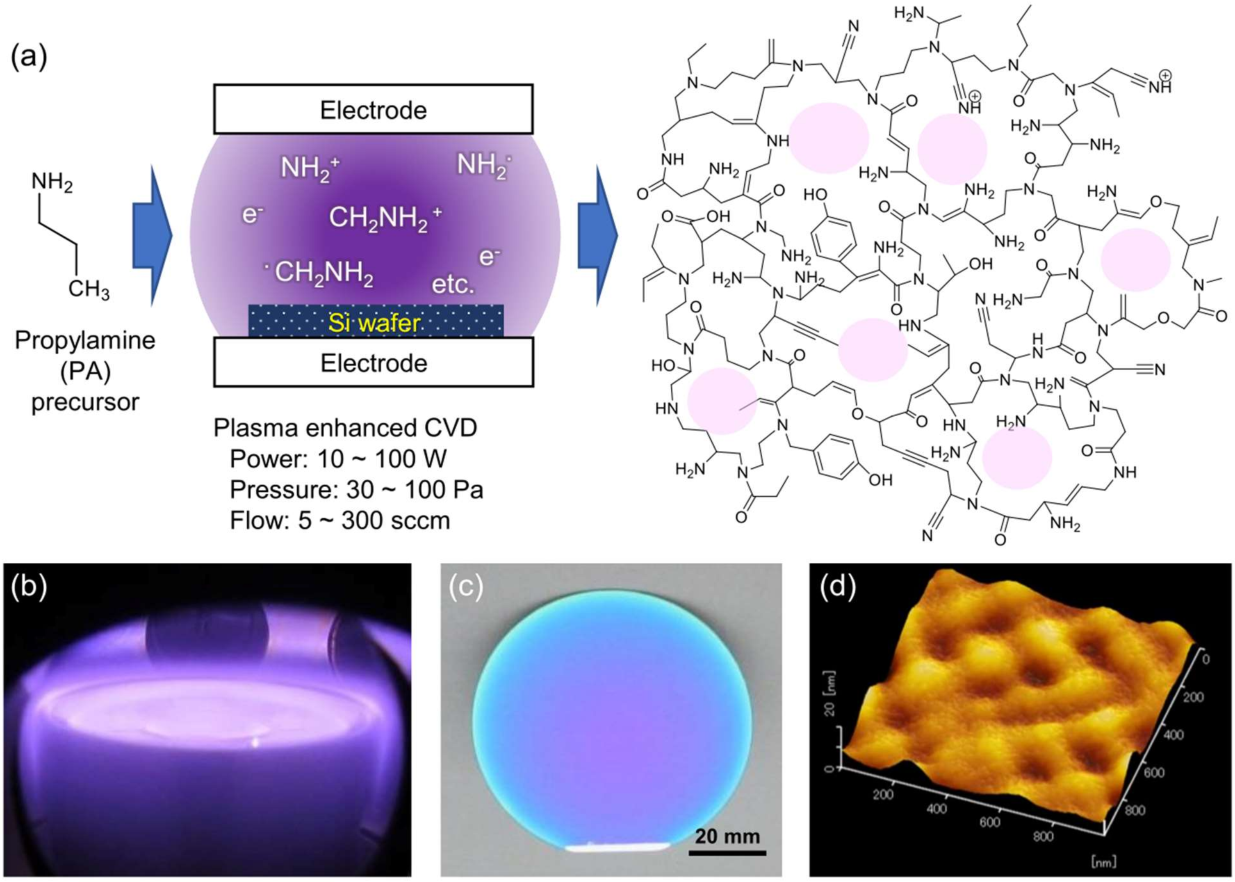

Fig. 1. (a) Schematic representation of PECVD using propylamine (PA) gas as a precursor. The plasma composition and final membrane structure were determined by MS, elemental analysis, FTIR, ^{13}C NMR, and titrimetry. Pores within the membrane's molecular framework are highlighted by pink circles. (b) Photograph of a PA plasma under typical condition (20 W, 50 Pa, 50 sccm). (c) Photograph of a PA-CVD membrane deposited on a silicon substrate. (d) An AFM image of a 100-nm thick PA-CVD membrane transferred onto a 200 nm porous

A PA plasma was generated by applying a 13.54 MHz high-frequency current through a 25 mm gap between an electrode and a counter electrode (⌀ 65 mm) (SI; Fig. S1). The PA gas introduced into the CVD chamber was decomposed into various ions, electrons, and radicals by the high-frequency (RF) power, and it emitted a strong purple light. The cationic species formed were identified by mass spectroscopic analysis of the plasma gas in the chamber. The major cations detected were $CH_2{=}NH_2^+$, $CH{\equiv}NH^+$, $CH_2{=}CH{-}CH_2^+$, and NH_2^+ (SI; Fig. S4) [58]. These cations should coexist with the corresponding radicals as well as protons, electrons, and other anionic species. Examples of the active species generated under our plasma conditions are shown in Fig. 1(a). The radicals and reactive species with multiple bonds polymerized to form densely crosslinked membranes on the Si substrate. The chemical structure of the PA-CVD membrane is shown schematically in Fig. 1(a).

Figure 1(b) shows a photograph of a plasma produced under our typical conditions. Emission of purple light due to the presence of nitrogen-based activated species was observed near the CVD electrode (lower electrode). The reactive plasma was constrained from expanding from the vicinity of the CVD electrode by the high pressure of the precursor gas (50 Pa) [59, 60]. When a 75-mm-diameter silicon substrate was placed on the CVD electrode, a PA-CVD membrane with a thickness of a few tens of nanometers was deposited within about one minute. Note that the initial plasma was in a nonequilibrium state and that the gas pressure increased for short while before reaching an equilibrium state within ten seconds. In general, the pressure increase due to the fragmentation of the precursor gas competes with the pressure decrease through the deposition of active species. In the case of propylamine gas, the initial pressure increased to 61.5 Pa and then decreased to 50 Pa. Figure 1(c) shows a photograph of a PA-CVD membrane deposited on a silicon substrate for 264 seconds. The constant interference color observed near the center of the 30-mm-diameter sample indicated the deposition of a uniform membrane with a thickness of about 200 nm. As confirmed by optical microscopy, this PA-CVD membrane was homogeneous and flat without any texture as shown later. An AFM image of a PA-CVD membrane transferred onto a porous alumina substrate is shown in Fig. 1(d). Details of the transfer process are given in the SI (Fig. S5). The PA-CVD membrane had a high flexibility and the surface topography of the underlying alumina substrate could be clearly observed. As shown later, this is in contrast to Fig. 2(b), in which PA-CVD on Si wafer has a very flat surface.

3.2 Structural characterization

Figure 2(a) is a large-scale topographic image of a cross-section of a PA-CVD membrane deposited on a glass substrate for 66 seconds. The left-hand part of the substrate was covered with a mask to evaluate the thickness of the membrane. This color confocal microscopy image verified that the thickness was a highly constant 48 nm over the observed area of 1 × 1 mm^2. The thickness of the PA-CVD membrane deposited on the Si substrate under the same conditions was determined to be 56 nm by AFM measurements [Fig. 2 (b)]. The 8 nm increase in membrane thickness might have resulted from swelling during the transfer process. Figure 2(c) shows a cross-sectional SEM image of a 100-nm thick PA-CVD membrane transferred onto a porous alumina substrate. Part of the membrane had detached from the substrate, indicating that this soft membrane could be bent with a radius of curvature of less than 1 μm. We then compared the thicknesses of the PA-CVD membranes as estimated by confocal microscopy and by ellipsometry, respectively [Fig. 2(d)]. As measured by both methods, the thicknesses increased linearly with the deposition time. However, ellipsometry gave relatively greater values of the thickness than those obtained by confocal microscopy. The latter method seems to be useful for the evaluation of thicknesses of less than 50 nm. The slope of the linear fit gave a deposition rate of 0.74 nm s^{-1}.

The concentration of basic dissociative functional groups in a PA-CVD membrane was evaluated by back-titration with aqueous hydrochloric acid to be 4.35 mmol g^{-1}, more than double that of a typical anion-exchange membrane (Please see Supporting Information, Section 6) [61, 62]. Back-titration with aqueous sodium hydroxide solution gave a total of acidic dissociative groups of 0.94

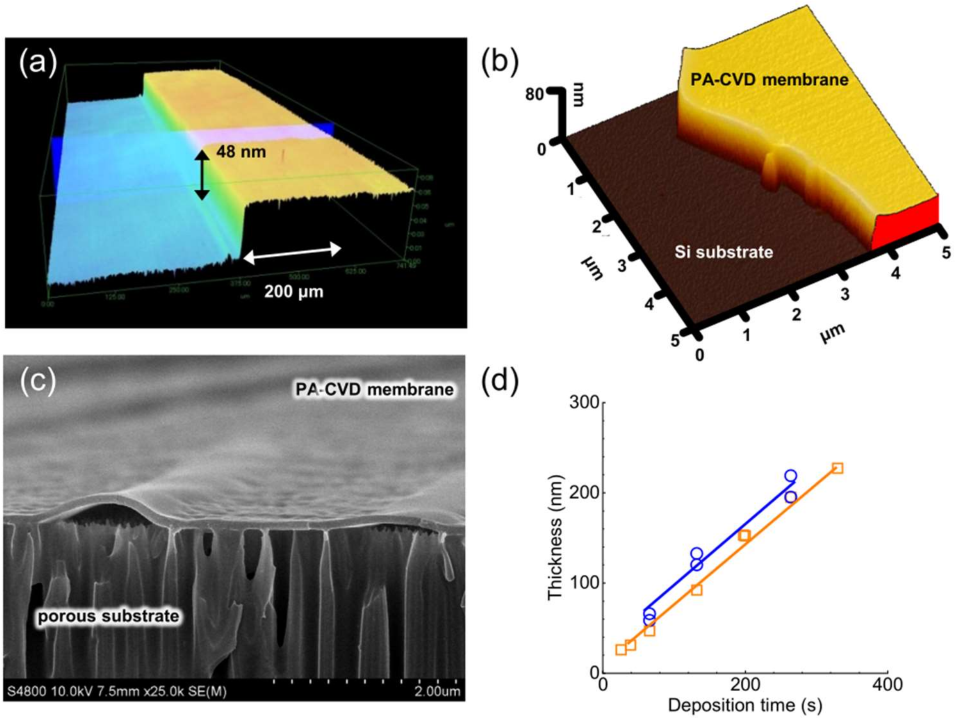

Fig. 2. (a) Large-scale topographic image of a cross-section of a PA-CVD membrane deposited on a glass substrate. Imaging area: 1 × 1 mm^2. (b) AFM image of the same membrane deposited on Si wafer. Imaging area: 5 × 5 μm^2. (c) Cross-sectional SEM image of the membrane transferred on a porous alumina substrate. (d) Changes in the thickness of PA-CVD membranes as a function of the deposition time. The thickness was determined by confocal microscopy (squares) or spectroscopic ellipsometry (circles). The CVD membrane was deposited under typical conditions (20 W, 50 Pa, 50 sccm).

mmol g^{-1}, consisting of 0.62 mmol g^{-1} of phenolic hydroxy groups and 0.32 mmol g^{-1} carboxylic acid groups. Because the PA-CVD membrane contains 4.6 times more basic dissociative groups than acidic ones, the membrane becomes positively charged in neutral water.

For elemental analysis, we prepared a sample of a PA-CVD membrane a few micrometers thick by deposition for several hours under typical conditions (20 W, 50 Pa, 50 sccm). The resultant membrane had a composition of $C_3H_{4.7}N_{0.8}O_{0.4}$, indicating that large numbers of oxygen atoms were introduced into the membrane and that the carbon/nitrogen ratio was close to that in the original precursor gas (C_3H_9N). We also observed a large decrease in the number of hydrogen atoms due to preferential detachment from the precursor fragments generated by collisions with high-energy electrons in the plasma state.

We analyzed the results of the elemental analyses and titration experiments to estimate the structure of the functional groups in the membrane. By simply assuming that all the basic functional groups were amino groups, 32% of the nitrogen atoms in the membrane were calculated to be dissociative. Phenolic hydroxy groups accounted for 9% of the oxygen atoms. Because each carboxylic acid group contains two oxygen atoms, 10% of the oxygen atoms in the membrane were assigned to dissociative carboxylic acid groups.

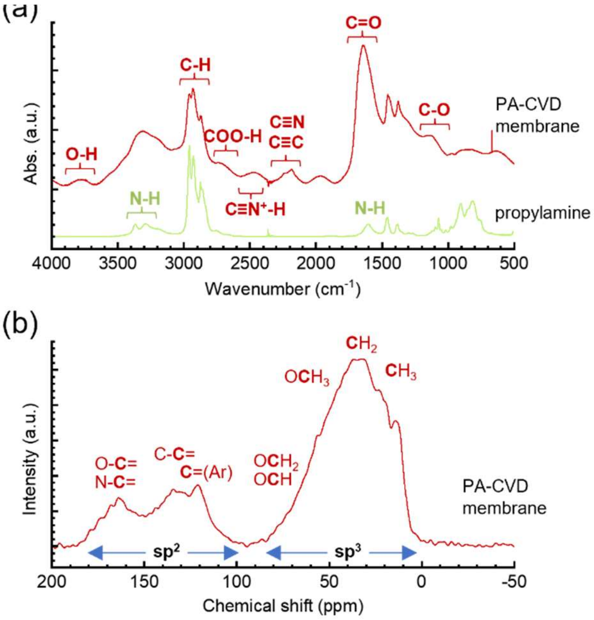

Fig. 3. (a) FTIR spectra of a PA-CVD membrane and the propylamine monomer. (b) ^{13}C NMR spectrum of a PA-CVD membrane.

Figure 3(a) shows FTIR spectra of a PA-CVD membrane and its propylamine precursor. The vibration peaks of methyl, methylene, and primary amino groups can be clearly observed in both spectra. In addition to these, the spectra show weak absorption peaks at 2185 and 2240 cm^{-1}, suggesting that the PA-CVD membrane contained carbon–carbon triple bonds and nitrile groups, respectively. The large peak at 1645 cm^{-1} and the broad peak near 1138 cm^{-1} were attributed to carbonyl groups of amide structures and to C–O bonds in ester groups, respectively. The broad absorption band near 3400 cm^{-1} was assigned to N–H groups and adsorbed water molecules. The PA-CVD membrane also produced a broad peak at 3700–3800 cm^{-1}, indicating the presence of isolated phenolic hydroxy groups. Furthermore, the presence of highly reactive species was suggested by the presence of the broad band at 2400–2800 cm^{-1}, which was unstable and, in general, gradually disappeared upon aging [63, 64]. The results of FTIR and elemental analysis clarified that the PA-CVD membrane contained abundant carbonyl and hydroxy groups.

The ^{13}C NMR spectrum of the PA-CVD membrane is shown in Fig. 3(b). Broad overlapping signals for a methyl peak at 11 ppm and a methylene peak near 34 ppm were observed. Methylene groups appeared to form the major carbon component of the PA-CVD membrane, but the broad tailing between 50 and 80 ppm corresponds to methyl and methylene groups bonded to oxygen. The peaks at 120 and 135 ppm were attributed to sp^2 carbons. The signal near 165 ppm was assigned to sp^2 carbons bonded to nitrogen or oxygen. The existence of sp^2 carbons indicated the formation of partial conjugated structures within the PA-CVD membrane.

From these compositional and structural analyses, we conclude that the PA-CVD membrane contained various unsaturated structures produced from dehydrogenated propylamine fragments. A PA-CVD membrane immediately after deposition retains large numbers of radicals that react with oxygen upon exposure to air to form ester, ketone, and acidic groups. The UV-vis spectrum of a PA-CVD membrane showed almost no absorbance within the visible-light region, but the absorbance increased exponentially at wavelengths of less than 400 nm. This also supports the formation of localized conjugated structures.

Unsaturated hydrocarbons such as acetylene have been widely used in producing high-strength carbon membranes by CVD techniques [34, 65-67]. On the other hand, saturated hydrocarbons produce densely crosslinked membranes containing hydrogen [68]. In this case, radicals within the membranes remain and some of them are oxidized by oxygen, although the membrane retains its hydrophobicity. When we deposited a thin carbon film from propane onto a Si substrate, we found that the water contact angle was 95°, whereas the water contact angle of our PA-CVD membrane was 43°. The hydrophilicity of the PA-CVD membrane originates mainly from the presence of amino groups.

Figure 4(a) shows a TEM image of 100-nm-thick PA-CVD membrane transferred on to a copper grid. The diffraction pattern in the inset was completely featureless, indicating that the membrane had an amorphous structure. In contrast, PALS revealed the existence of subnanoscale pores in the PA-CVD membrane, as the spectra showed significant intensities in the range 4 to 10 ns. By fitting the

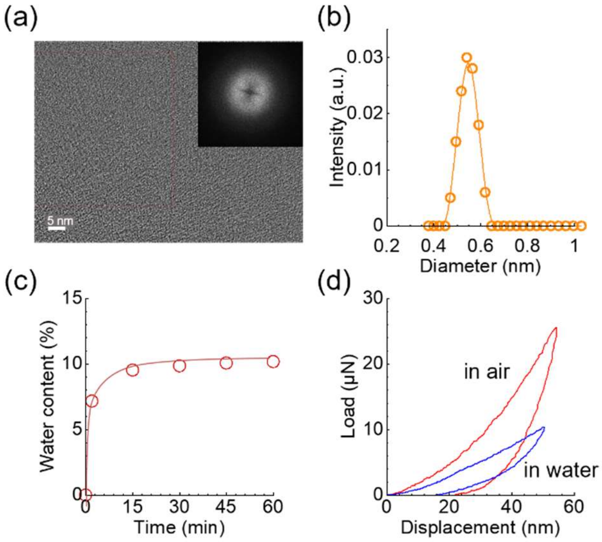

Fig. 4. (a) TEM image of a 100-nm thick PA-CVD membrane transferred onto a copper grid. (b) Pore-size distribution curve obtained by PALS analysis. The distribution was calculated from the spectrum by using the CONTIN algorithm. (c) Changes in the water content of a PA-CVD membrane with water-immersion time. (d) Load-displacement curves measured by using a nanoindentometer.

PALS spectra using the exponential decay of three lifetime components, we determined the longest lifetime to be 1.87 ns. By using a semiempirical equation reported in the literature [57], we calculated that the average pore diameter in the membrane (deposition time: 300 s) was 0.54 nm. PALS data were also evaluated by using a CONTIN algorithm based on the inverse Laplace transform [57]. Fig. 4(b) is a plot of the pore-size distribution curve. The pore diameter at the peak was 0.54 nm, which is consistent with the average pore diameter determined by the semiempirical method. The maximum pore diameter in the distribution was 0.64 nm, which is much larger than the size of a water molecule (0.30 nm) and slightly smaller than the hydration diameter of a sodium ion (0.72 nm) [69]. As mentioned later, a 100-nm-thick PA-CVD membrane deposited under the same conditions showed an NaCl retention factor of more than 90%.

Hydrophilic PA-CVD membranes sorb water molecules and expand slightly. To estimate the water-sorption capacity, we measured the thickness and refractive index of a PA-CVD membrane immersed in water by using a spectroscopic ellipsometer. Fig. 4(c) is a plot of the changes in water content against the immersion time, where the water content was calculated from the change in thickness (Fig. S3). The membrane swelled rapidly in water and became saturated at a water content of about 10%. We also confirmed that a decrease in the refractive index occurred due to the decrease in the density of the membrane.

The PA-CVD membrane became soft in water. The results of nanoindentation measurements are shown in Fig. 4(d). The hardness in water was about one-third of the value in air. The Young's modulus (E_r) in the dry state was determined to be 7.3 GPa, and this decreased to 2.6 GPa in the wet state. A decrease in Young's modulus has been frequently reported as an effect of plasticization by water molecules [70]. Water molecules block the chemical interactions that are present in dried PA-CVD membranes, thereby facilitating deformation. The relationship between stress (σ) and strain (ε) is given by the following equation:

$\varepsilon = \sigma/E,$

where E is the Hooke's law elastic modulus. If we assume that E is equal to E_r (2.6 GPa) and σ is 10 MPa (100 atm of applied pressure), the value of ε is as little as 0.38%. This means that the compressibility of the PA-CVD membrane under a high pressure is very low, so that this membrane is sufficiently strong for use as pressure-driven separation membrane.

3.3 Deposition behavior

We prepared PA-CVD membranes under various deposition conditions and determined their average pore diameters, d_3, and intensities, I_3, from the long-lifetime component (third component) measured by PALS (SI; Table S2). Fig. 5(a) shows a plot of the changes in d_3 and I_3 against the input power during deposition at 50 Pa and 50 sccm, where the I_3 represents the percentage of the third-lifetime component. The deposition time was 132 s. The average pore size of 0.62 nm at 10 W gradually decreased to 0.43 nm when input power was increased to 40 W. The I_3 value of 18.2% at 10 W decreased exponentially to 0.7% when the input power was increased to 40 W. In other words, the pore

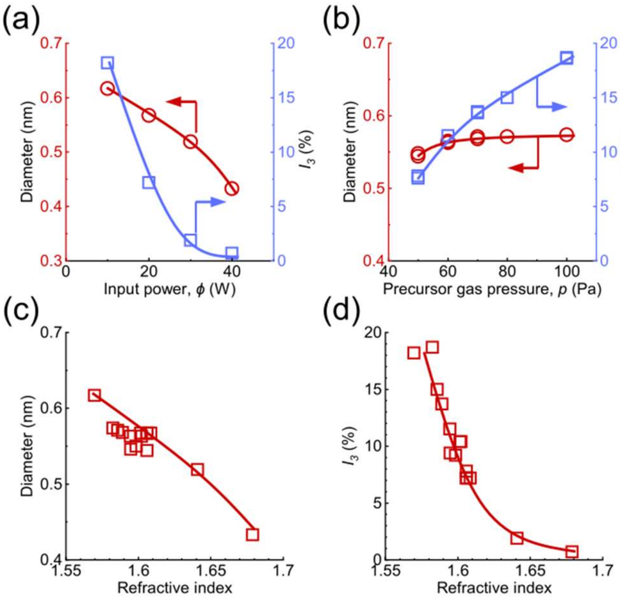

Fig. 5. (a, b) Pore diameter and its percentage (I_3) measured with PALS as a function of input power (ϕ) and precursor-gas pressure (p). (c, d) The relation of pore diameter and I_3 percentage to the refraction index of PA-CVD membrane.

volume of PA-CVD membrane decreased markedly upon increasing the input power. Fig. 5(b) shows plots of d_3 and I_3 against the precursor-gas pressure. The flow rate of the precursor gas, the input power, and the deposition time of the PA-CVD membrane were 50 sccm, 20 W, and 264 s, respectively. Although the pore size slightly increased with increasing precursor-gas pressure, it was still 0.57 nm, even at 100 Pa. The I_3 values increased monotonically with precursor-gas pressure, reaching 18.7% at 100 Pa. Pore volume increased with increasing precursor-gas pressure. The density of the PA-CVD membrane can be evaluated from a linear correlation with the refractive index as obtained by using a spectroscopic ellipsometer. The relationships between the refractive index and d_3 and I_3 are plotted in Figs. 5(c) and 5(d), respectively. The pore sizes were concentrated between 0.5 and 0.6 nm, and these membranes had a refractive index of about 1.6. Note that this range of refractive index was about 20% larger than that of aromatic polymers. When the pore size became extremely small, the refraction index also increased. On the other hand, I_3 and the refractive index had a reciprocal relationship; the value of I_3 in the membrane decreased significantly with increasing refractive index. We also confirmed that low-density membranes (with low refractive index) have a high deposition rate of 4.1 nm s^{-1} (SI; Fig. S9).

To evaluate its separation performance, the PA-CVD membrane must be directly prepared on a porous support layer. Also, the separation functional layer should be as thin as possible to achieve a high filtration performance. This requires a deep understanding of the coverage mechanism and the speed of deposition of the PA-CVD membrane on nanopores. Fig. 6(a) shows PA-CVD membranes deposited on porous alumina substrates. The growth of the membrane began from the framework of

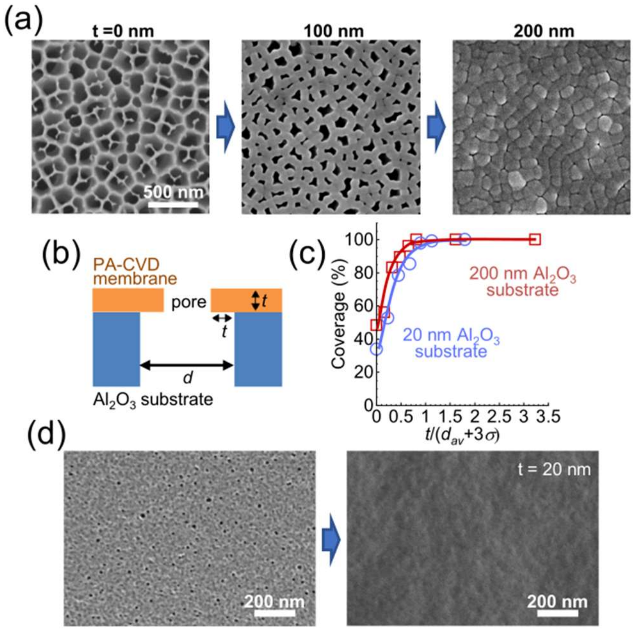

Fig. 6. (a) SEM images of PA-CVD membranes on 200 nm pores of porous alumina substrate with increasing deposition thickness (*t*). (b) Schematic illustration of growth of PA-CVD membrane on a porous substrate. (c) Surface coverage on 20 or 200 nm pores of alumina substrates as a function of $t/(d_{av}+3\sigma)$. d_{av}: average pore diameter of the substrate, σ: standard deviation of pore size distribution of the substrate. The σ values of the 20-nm and 200-nm pore alumina substrates are 8.5 and 27.3, respectively. (d) SEM images before and after deposition of a 20-nm thick PA-CVD membrane on a PPSU substrate.

the porous substrate. The 200-nm pores were subsequently completely covered by a 200-nm-thick PA-CVD membrane. Under our deposition conditions, the precursor-gas pressure was 10 times higher as compared to our previous report [34], and then the mean free path of the reactive species was short, so that the increase in membrane thickness and the rate of pore closure were almost the same. This growth is shown schematically in Fig. 6(b). In this model, the pore diameter of the porous alumina substrate decreases linearly with increasing thickness of the PA-CVD membrane. When the closing pore diameter (*d*) was normalized by the initial average pore diameter (d_{av}) of the porous substrate and plotted against the thickness of PA-CVD membrane, the d/d_{av} values decreased linearly. If we assume that the pore diameter of the alumina substrate follows a Gaussian distribution, 99.7% of the pores are contained within the range d_{av} + 3σ, where σ is the standard deviation. Fig. 6(c) shows a plot of the coverage of the porous alumina substrate against the thickness (t) of the PA-CVD membrane normalized by $d_{av} + 3\sigma$. The coverage increased monotonically with the growth of membrane thickness and reached almost 100% when the membrane thickness exceeded $d_{av} + 3\sigma$. To cover pores with a Gaussian pore distribution, a membrane thickness of $d_{av} + 3\sigma$ is required. In the case of an asymmetric PPSU membrane prepared by a non-solvent-induced phase-separation method (SI; Fig. S6), the 20 nm pores on the surface were entirely covered by the 20-nm-thick PA-CVD membrane [Fig. 6(d)]. A denser asymmetric membrane can, therefore, be covered with a further thinner PA-CVD membrane.

3.4 Separation performance

Figure 7(a) shows the retention of alcohols by a 230-nm-thick PA-CVD membrane deposited on a PPSU substrate. The retention factors were evaluated by filtering 0.1 wt% aqueous alcohol solution through a high-pressure dead-end filtration setup. The alcohol concentration in the filtrate was measured by gas chromatography. For primary alcohols, the retention factor increased with increasing

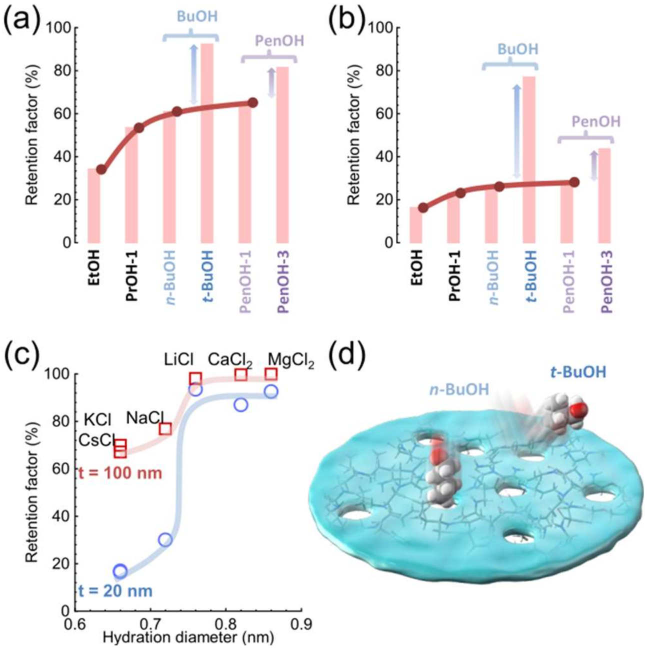

Fig. 7. Retention factors of alcohol molecules by (a) 230-nm-thick and (b) 50-nm-thick PA-CVD membranes. The permeances for water were about 0.5 and 1.7 L m^{-2} h^{-1} bar^{-1}, respectively. (c) Retention factors of inorganic salts by 20-nm- and 100-nm-thick PA-CVD membranes. (d) Schematic representation of a PA-CVD membrane with pores rejecting *tert*-butanol but permitting the passage of *n*-butanol. Please see Fig. S8 (a) for the flux data, and Table S2 for pore size data.

molecular weight from ethanol through pentanol. The retention factors of *n*-butanol and 1-pentanol were 61% and 65%, respectively. In contrast, the retention factors of *tert*-butanol and 3-pentanol increased to 92% and 82%, respectively. The pores of the PA-CVD membrane can therefore discriminate between alcohol isomers. The retention factors of the 50-nm-thick PA-CVD membrane are shown in Fig. 7(b). As the membrane thickness decreased, the retention factors for alcohols also decreased, but the difference in the retention of the isomers became greater. The retention factors of *n*-butanol and 1-pentanol were 26% and 28%, respectively. These results show that the permeability toward linear alcohol molecules is almost constant.

We evaluated the retention performance of nine types of C4 and C5 alcohols, such as 2-butanol, 2-pentanol, 3-methyl-1-butanol, 2-methyl-1-propanol, and 2,2-dimethyl-1-propanol. Their structures and retention factors are compiled in Fig. S7 and Table S3 of the SI. The retention factors of C4 alcohols increased in the order *n*-butanol < 2-butanol < 2-methyl-1-propanol < *tert*-butanol; whereas those of C5 alcohols increased in the order 1-pentanol < 3-pentanol < 2-pentanol < 3-methyl-1-butanol < 2,2-dimethyl-1-propanol. All these results can be explained in terms of the degree of bulkiness (also known as the Stokes radius) of the alcohol molecules (Please see Table S3 in Supporting Information). The Stokes radius has positive relationship with retention factors of alcohol molecules.

For comparison, the retention factors of six salts were plotted with the size of their hydrated cations on the abscissa [Fig. 7(c)] [69]. As the membrane thickness decreases from 100 to 20 nm, the retention of small cations decreased, but retention factors remained high for ions with hydrated diameters larger than 0.75 nm. These results indicate that the PA-CVD membrane does not contain penetrating pores larger than 0.75 nm, and a size-selective separation is occurring. We believe the PA-CVD membrane is elastic, and slightly swells and extends under pressure. These tendencies are significant in thinner membranes. That is, sub-nanometer pores in 20-nm-thick membrane are relatively readily swollen in water and expanded in pressure driven filtration as compared to the 100-nm-thick membrane. The flux of the PA-CVD membrane obeyed the Hagen–Poiseuille equation; that is, the flux was proportional to the pressure and inversely proportional to the membrane thickness. The flux for the 20-nm-thick membrane at 4 MPa reached 170 L m^{-2} h^{-1} (SI; Fig. S8). From all these results, we can simply conclude that penetrating pores formed in the PA-CVD membrane are able of discriminating subtle size differences of alcohols. This retention is shown schematically in Fig. 7(d).

3.5 Porosity control

The pore size of the PA-CVD membranes was significantly affected by the plasma power. For example, the average pore size varied between 0.62 and 0.43 nm when the input power was changed from 10 to 40 W (SI; Table S2) when the flow rate and the pressure were fixed at 50 sccm and 50 Pa, respectively. We systematically investigated the effects of deposition parameters and we characterized the membranes by using an optical ellipsometer equipped with a liquid cell. Figure 8(a) shows the relationship between the input power, ϕ, and the refraction index of the membranes. At a precursor-gas pressure, p, of 50 Pa, the refractive index was 1.56 at an input power of 10 W but increased to 2.00

when the power was raised to 100 W. Under these conditions, the refractive index increased linearly with the input power. The refractive indices of PA-CVD membranes deposited at 30 Pa were slightly higher than those prepared at 50 Pa and reached a value of 2.0 at input powers above 70 W. As the precursor gas pressure increased, the membrane became less dense because of the decreased extent of the decomposition at the same power condition.

When the flow rate was low (10 sccm), the refractive index became relatively high [Fig. 8(b)]. Because the residence time of the precursor gas increases with decreasing flow rate, the decomposition of propylamine proceeds to a greater extent. Consequently, the resultant membrane becomes much denser. Judging from the fact that the refractive index of diamond-like carbon membranes is about 1.9 [71, 72], the membranes obtained at a high input power (70−100 W) must consist of dense amorphous carbon. In fact, the membranes showed almost no water absorption when prepared at input powers above 40 W [Fig. 8(c)]. The curve for water content sharply increased when the input power was below 20 W and exceeded 30% at 10 W. This indicates that the water permeability of PA-CVD membranes can be controlled over a wide range by altering the input power.

The refractive index increased monotonically when plotted against the inverse of the precursor-gas flow rate [Fig. 8(d)]. The reciprocal of the flow rate represents the residence time, indicating that a

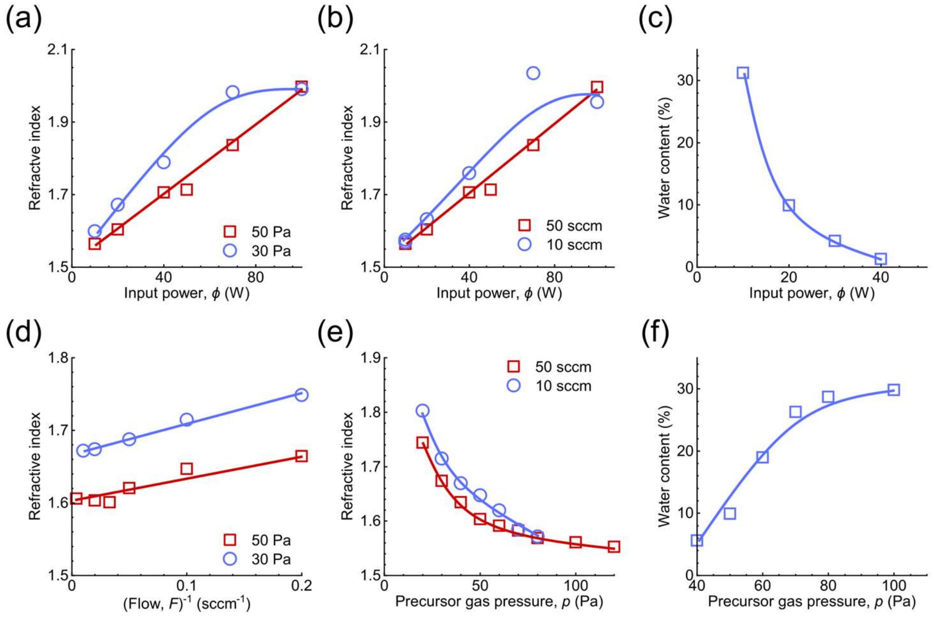

Fig. 8. (a, b) Refractive index of PA-CVD membranes as a function of input power (ϕ). The flow rate in (a) was 50 sccm. The precursor-gas pressure (p) in (b) was 50 Pa. (c) Water content as a function of the input power (ϕ) (50 sccm, 50 Pa). (d, e) Refractive index as a function of the inverse flow rate (F^{-1}) and the precursor-gas pressure, respectively. The input power was 20 W. (f) Water content as a function of the precursor-gas pressure (50 sccm, 20 W).

longer residence time leads to further decomposition of propylamine. However, by comparing the data at 50 and 30 Pa, we can conclude that the effect of the precursor-gas pressure is much greater than that of the residence time. The refractive index of PA-CVD membrane was inversely proportional to the precursor-gas pressure [Fig. 8(e)]. The coexistence of excess propylamine in the plasma gas is effective in forming a relatively low-density PA-CVD membrane. Figure 8(f) shows that the water content of the membrane increased markedly with increasing precursor-gas pressure in the plasma, reaching 30% at 100 Pa.

The deposition rate of PA-CVD membranes prepared at 50 Pa and 50 sccm increased with input power from 1.0 nm s^{-1} at 20 W to 2.6 nm s^{-1} at 40 W and 4.1 nm s^{-1} at 100 W (SI; Fig. S9). On the other hand, at 20 W and 50 sccm, the deposition rate decreased to 0.4 nm s^{-1} when the pressure was 120 Pa. The PA-CVD membrane with low density and a high water content grows relatively slowly.

The structure of PA-CVD membrane depends significantly on the deposition parameters. The effects of the deposition parameters on the membrane characteristics are summarized in Fig. 9. Increasing the input power yields densely crosslinked PA-CVD membranes. The crosslinking density further increased at above 40 W, and membranes obtained at above 70 W resembled diamond-like carbon. Conversely, at 10 W, 50 sccm, and 50 Pa, the average pore size became 0.62 nm. As with the input power, the effect of the precursor-gas pressure is significant, that is, high-pressure conditions result in PA-CVD membranes with high porosity.

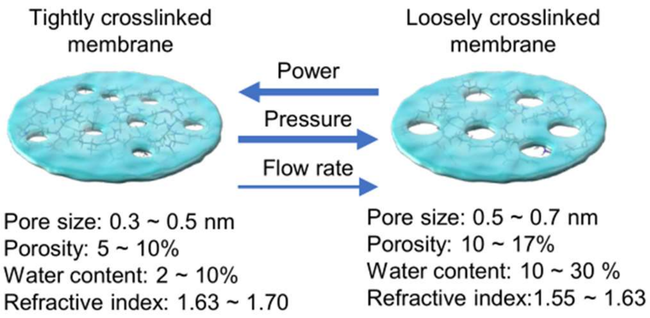

Fig. 9. Pore-size control of PA-CVD membranes by three plasma-process parameters and the ranges of membrane properties.

Increases in both the pressure and flow rate reduce the crosslinking density, but the influence of the pressure is much more significant. In particular, when the pressure was increased to 100 Pa, the membrane sorbs the water up to a content of 30%. By assuming a tortuosity of about 1.5 for the penetrating pores (⌀ 0.56 nm), we calculated the porosity from the Hagen–Poiseuille equation (SI; Fig. S8). As a result, we estimated that 7.7% of the surface of a 100-nm-thick PA-CVD membrane consists of pores. The porosity increases with increasing pressure of the precursor gas. The water content of the membrane varied most with the input power and the pressure. This indicates that the extent of decomposition of the propylamine precursor gas changes markedly according to the deposition parameters, resulting in a wide range of crosslinking densities.

4. Conclusions

Hydrophilic PA-CVD membranes with subnanometer pores were prepared by the PECVD method with propylamine as the precursor. The size and porosity of the membrane's nanopores can be controlled by an appropriate selection of the input power and the pressure and flow rate of the precursor gas. The relationships between these parameters and the structure and properties of the resulting membranes were investigated in detail. PA-CVD membranes prepared on an asymmetric substrate membrane completely rejected bivalent ions. The subnanometer pores accurately discriminated between alcohols of different molecular sizes, showing exceptional permeation selectivity toward isomers of C4 and C5 alcohols. In the case of a 50-nm-thick PA-CVD membrane, the retention factor of *tert*-butanol was three times higher than that of *n*-butanol. Compared with literature values, the permeance (1.2 L m^{-2} h^{-1} bar^{-1}) was 1/3.6 of that of polyamide membranes, but the selectivity was 2.5 times larger (SI; Fig. S10) [73-76]. On the other hand, a 20-nm-thick membrane had a high water flux of 170 L m^{-2} h^{-1} at a pressure differential of 40 bar. These PA-CVD membranes therefore showed a good performance balance of flux and selectivity as alcohol-separation membranes (SI; Table S4). The deposition rate of PA-CVD membrane could be controlled in the range 0.5–2.0 nm s^{-1}. High retention of divalent cations was observed, even for the 10-nm-thick membrane, due to its high density of positive charges. The preparation of thinner membranes would be possible by using substrates with smaller pores. The water content could also be controlled over a wider range to improve the membrane's separation performance. The results of our study should contribute to the design of various plasma CVD membranes and the prediction of the performance of separation membranes.

CRediT authorship contribution statement

S. Samitsu: Methodology, Investigation, Formal analysis, Writing - Original Draft. **E. Ismail**: Writing - Review & Editing. **Y. Fujii**: Investigation. **I. Ichinose**: Supervision, Writing - Review & Editing

Acknowledgement

This work was partially supported by JSPS KAKENHI Grant Numbers 21H02006 and 22H02149, the Nippon Sheet Glass Foundation for Materials Science & Engineering, and the MOONSHOT R&D program JPJ009237. This was also supported by the COI Program "Global Aqua Innovation Center for Improving Living Standards and Water-sustainability" from JST. We thank TEM station and NAMIKI foundry at NIMS for instrumental support for TEM and spectroscopic ellipsometry, respectively. We also thank Hitachi High-Tech for support on the high-resolution cross-sectional SEM images.

References

[1] S.P. Nunes, K.-V. Peinemann, Membrane Technology: In the Chemical Industry, Wiley-VCH, Weinheim, 2001. https://doi.org/10.1002/3527600388.

[2] S. Gray, T. Tsuru, Y. Cohen, W.-J. Lau (Eds.), Advanced Materials for Membrane Fabrication and Modification, CRC Press, Boca Raton, 2018. https://doi.org/10.1201/9781315184357.

[3] R.W. Baker, Membrane Technology and Applications, third ed., Wiley, Chichester, 2012. https://doi.org/10.1002/9781118359686.

[4] S. Karan, Z. Jiang, A.G. Livingston, Sub-10 nm polyamide nanofilms with ultrafast solvent transport for molecular separation, Science 348 (2015) 1347–1351. https://doi.org/10.1126/science.aaa5058.

[5] D.F. Sanders, Z.P. Smith, R. Guo, L.M. Robeson, J.E. McGrath, D.R. Paul, B.D. Freeman, Energy-efficient polymeric gas separation membranes for a sustainable future: A review, Polymer 54 (2013) 4729–4761. https://doi.org/10.1016/j.polymer.2013.05.075.

[6] H. Sanaeepur, A. Ebadi Amooghin, S. Bandehali, A. Moghadassi, T. Matsuura, B. Van der Bruggen, Polyimides in membrane gas separation: Monomer's molecular design and structural engineering, Prog. Polym. Sci. 91 (2019) 80–125. https://doi.org/10.1016/j.progpolymsci.2019.02.001.

[7] Y. Liang, Y. Zhu, C. Liu, K.R. Lee, W.S. Hung, Z. Wang, Y. Li, M. Elimelech, J. Jin, S. Lin, 2020. Polyamide nanofiltration membrane with highly uniform sub-nanometre pores for sub-1 A precision separation, Nat. Commun. 11, 2015. https://doi.org/10.1038/s41467-020-15771-2.

[8] Y. Wei, Y. Zhang, X. Gao, Z. Ma, X. Wang, C. Gao, Multilayered graphene oxide membranes for water treatment: A review, Carbon 139 (2018) 964–981. https://doi.org/10.1016/j.carbon.2018.07.040.

[9] K. Nakagawa, S. Araya, K. Ushio, M. Kunimatsu, T. Yoshioka, T. Shintani, E. Kamio, K.-L. Tung, H. Matsuyama, 2021. Controlling interlayer spacing and organic solvent permeation in laminar graphene oxide membranes modified with crosslinker, Sep. Purif. Technol. 276, 119279. https://doi.org/10.1016/j.seppur.2021.119279.

[10] K.H. Thebo, X. Qian, Q. Zhang, L. Chen, H.M. Cheng, W. Ren, 2018. Highly stable graphene-oxide-based membranes with superior permeability, Nat. Commun. 9, 1486. https://doi.org/10.1038/s41467-018-03919-0.

[11] Q. Yang, Y. Su, C. Chi, C.T. Cherian, K. Huang, V.G. Kravets, F.C. Wang, J.C. Zhang, A. Pratt, A.N. Grigorenko, F. Guinea, A.K. Geim, R.R. Nair, Ultrathin graphene-based membrane with precise molecular sieving and ultrafast solvent permeation, Nat. Mater. 16 (2017) 1198–1202. https://doi.org/10.1038/nmat5025.

[12] Y. Yang, X. Yang, L. Liang, Y. Gao, H. Cheng, X. Li, M. Zou, R. Ma, Q. Yuan, X. Duan, Large-area graphene-nanomesh/carbon-nanotube hybrid membranes for ionic and molecular nanofiltration, Science 364 (2019) 1057–1062. https://doi.org/10.1126/science.aau5321.

[13] M. Barrejón, M. Prato, 2021. Carbon nanotube membranes in water treatment applications, Adv. Mater. Interfaces 9, 2101260. https://doi.org/10.1002/admi.202101260.

[14] M.H. Rashid, S.F. Ralph (2017), Carbon nanotube membranes: Synthesis, properties, and future filtration applications, Nanomaterials 7, 99. https://doi.org/10.3390/nano7050099.

[15] S. Huang, M. Dakhchoune, W. Luo, E. Oveisi, G. He, M. Rezaei, J. Zhao, D.T.L. Alexander, A. Züttel, M.S. Strano, K.V. Agrawal, 2018. Single-layer graphene membranes by crack-free transfer for

gas mixture separation, Nat. Commun. 9, 2632. https://doi.org/10.1038/s41467-018-04904-3.

[16] L. Wang, M.S.H. Boutilier, P.R. Kidambi, D. Jang, N.G. Hadjiconstantinou, R. Karnik, Fundamental transport mechanisms, fabrication and potential applications of nanoporous atomically thin membranes, Nat. Nanotechnol. 12 (2017) 509–522. https://doi.org/10.1038/nnano.2017.72.

[17] S. Li, R. Dong, V.-E. Musteata, J. Kim, N.D. Rangnekar, J.R. Johnson, B.D. Marshall, S. Chisca, J. Xu, S. Hoy, B.A. McCool, S.P. Nunes, Z. Jiang, A.G. Livingston, Hydrophobic polyamide nanofilms provide rapid transport for crude oil separation, Science 377 (2022) 1555–1561. https://doi.org/10.1126/science.abq0598.

[18] W. Ma, M. Zhang, Z. Liu, M. Kang, C. Huang, G. Fu, Fabrication of highly durable and robust superhydrophobic-superoleophilic nanofibrous membranes based on a fluorine-free system for efficient oil/water separation, J. Membr. Sci. 570–571 (2019) 303–313. https://doi.org/10.1016/j.memsci.2018.10.035.

[19] W. Kushida, R.R. Gonzales, T. Shintani, A. Matsuoka, K. Nakagawa, T. Yoshioka, H. Matsuyama, Organic solvent mixture separation using fluorine-incorporated thin film composite reverse osmosis membrane, J. Mater. Chem. A 10 (2022) 4146–4156. https://doi.org/10.1039/d1ta09192a.

[20] T. Aida, E.W. Meijer, S.I. Stupp, Functional supramolecular polymers, Science 335 (2012) 813–7. https://doi.org/10.1126/science.1205962.

[21] Y. Itoh, S. Chen, R. Hirahara, T. Konda, T. Aoki, T. Ueda, I. Shimada, J.J. Cannon, C. Shao, J. Shiomi, K.V. Tabata, H. Noji, K. Sato, T. Aida, Ultrafast water permeation through nanochannels with a densely fluorous interior surface, Science 376 (2022) 738–743. https://doi.org/10.1126/science.abd0966.

[22] J. Wang, Z. Zhang, J. Zhu, M. Tian, S. Zheng, F. Wang, X. Wang, L. Wang, 2020. Ion sieving by a two-dimensional $Ti_3C_2T_x$ alginate lamellar membrane with stable interlayer spacing, Nat. Commun. 11, 3540. https://doi.org/10.1038/s41467-020-17373-4.

[23] A.W. Mohammad, Y.H. Teow, W.L. Ang, Y.T. Chung, D.L. Oatley-Radcliffe, N. Hilal, Nanofiltration membranes review: Recent advances and future prospects, Desalination 356 (2015) 226–254. https://doi.org/10.1016/j.desal.2014.10.043.

[24] F. Russo, F. Galiano, A. Iulianelli, A. Basile, A. Figoli, Biopolymers for sustainable membranes in CO_2 separation: A review, Fuel Process. Technol. 213 (2021). https://doi.org/10.1016/j.fuproc.2020.106643.

[25] F. Seidi, A. Arabi Shamsabadi, A. Ebadi Amooghin, M.R. Saeb, H. Xiao, Y. Jin, M. Rezakazemi, Biopolymer-based membranes from polysaccharides for CO_2 separation: A review, Environ. Chem. Lett. 20 (2022) 1083–1128. https://doi.org/10.1007/s10311-021-01349-x.

[26] P. Marchetti, M.F. Jimenez Solomon, G. Szekely, A.G. Livingston, Molecular separation with organic solvent nanofiltration: A critical review, Chem. Rev. 114 (2014) 10735–10806. https://doi.org/10.1021/cr500006j.

[27] P. Vandezande, L.E. Gevers, I.F. Vankelecom, Solvent resistant nanofiltration: Separating on a molecular level, Chem. Soc. Rev. 37 (2008) 365–405. https://doi.org/10.1039/b610848m.

[28] A.O. Rashed, A. Merenda, T. Kondo, M. Lima, J. Razal, L. Kong, C. Huynh, L.F. Dumée, 2021. Carbon nanotube membranes: Strategies and challenges towards scalable manufacturing and practical separation applications, Sep. Purif. Technol. 257, 117929. https://doi.org/10.1016/j.seppur.2020.117929.

[29] B.J. Hinds, N. Chopra, T. Rantell, R. Andrews, V. Gavalas, L.G. Bachas, Aligned multiwalled carbon nanotube membranes, Science 303 (2004) 62–65. https://doi.org/10.1126/science.1092048.

[30] X.-H. Lin, J.-G. Gai, Synthesis and applications of large-area single-layer graphene, RSC Adv. 6 (2016) 17818–17844. https://doi.org/10.1039/c5ra27349h.

[31] K.R. Buck, V.K. Davar, Application of glow discharge polymerisation to the preparation of reverse osmosis membranes, Br. Polym. J. 2 (1970) 238–239. https://doi.org/10.1002/pi.4980020406.

[32] J.R. Hollohan, T. Wydeven, Synthesis of reverse osmosis membranes by plasma polymerization of allylamine, Science 179 (1973) 500–501. https://doi.org/10.1126/science.179.4072.500.

[33] H. Yasuda, C.E. Lamaze, Preparation of reverse osmosis membranes by plasma polymerization of organic compounds, J. Appl. Polym. Sci. 17 (1973) 201–222. https://doi.org/10.1002/app.1973.070170116.

[34] S. Karan, S. Samitsu, X. Peng, K. Kurashima, I. Ichinose, Ultrafast viscous permeation of organic solvents through diamond-like carbon nanosheets, Science 335 (2012) 444–447. https://doi.org/10.1126/science.1212101.

[35] T. Ohba, K. Kaneko, M. Endo, K. Hata, H. Kanoh, Rapid water transportation through narrow one-dimensional channels by restricted hydrogen bonds, Langmuir 29 (2013) 1077–1082. https://doi.org/10.1021/la303570u.

[36] Y. Tao, M. Endo, M. Inagaki, K. Kaneko, Recent progress in the synthesis and applications of nanoporous carbon films, J. Mater. Chem. 21 (2011) 313–323. https://doi.org/10.1039/c0jm01830a.

[37] J. Miyamoto, Y. Hattori, D. Noguchi, H. Tanaka, T. Ohba, S. Utsumi, H. Kanoh, Y.A. Kim, H. Muramatsu, T. Hayashi, M. Endo, K. Kaneko, Efficient H_2 adsorption by nanopores of high-purity double-walled carbon nanotubes, J. Am. Chem. Soc. 128 (2006) 12636–12637. https://doi.org/10.1021/ja064744+.

[38] H. Nagasawa, Y. Yamamoto, N. Tsuda, M. Kanezashi, T. Yoshioka, T. Tsuru, Atmospheric-pressure plasma-enhanced chemical vapor deposition of microporous silica membranes for gas separation, J. Membr. Sci. 524 (2017) 644–651. https://doi.org/10.1016/j.memsci.2016.11.067.

[39] H. Nagasawa, R. Yasunari, M. Kawasaki, M. Kanezashi, T. Tsuru, Atmospheric-pressure PECVD synthesis of polymer-supported molecular sieving silica membranes for gas separation: Effect of pore size of polymeric support, Mater. Lett. 308 (2022). https://doi.org/10.1016/j.matlet.2021.131211.

[40] L. Kleines, M. Jaritz, S. Wilski, J. Rubner, M. Alders, M. Wessling, C. Hopmann, R. Dahlmann, Enhancing the separation properties of plasma polymerized membranes on polydimethylsiloxane substrates by adjusting the auxiliary gas in the PECVD processes, J. Phys. D: Appl. Phys. 53 (2020). https://doi.org/10.1088/1361-6463/aba296.

[41] L.-J. Wang, F.C.-N. Hong, Carbon-based molecular sieve membranes for gas separation by

inductively-coupled-plasma chemical vapor deposition, Microporous Mesoporous Mater. 77 (2005) 167–174. https://doi.org/10.1016/j.micromeso.2004.09.001.

[42] A. Kakaroglou, B. Nisol, K. Baert, I. De Graeve, F. Reniers, G. Van Assche, H. Terryn, Evaluation of the Yasuda parameter for the atmospheric plasma deposition of allyl methacrylate, RSC Adv. 5 (2015) 27449–27457. https://doi.org/10.1039/c5ra02684a.

[43] H. Yasuda, T. Hirotsu, Polymerization of organic compounds in an electrodeless glow discharge. VIII. Dependence of plasma polymerization of acrylonitrile on glow characteristic, J. Appl. Polym. Sci. 21 (1977) 3139–3145. https://doi.org/10.1002/app.1977.070211124.

[44] H. Yasuda, Plasma Polymerization, Academic Press, Orlando, 1985. https://doi.org/10.1016/c2012-0-01688-2.

[45] J. Carneiro de Oliveira, A. Airoudj, P. Kunemann, F. Bally-Le Gall, V. Roucoules, 2021. Mechanical properties of plasma polymer films: A review, SN Appl. Sci. 3, 656. https://doi.org/10.1007/s42452-021-04655-9.

[46] M. Toda, K. Miyake, L.Q. Chu, M. Zakerin, R. Förch, R. Berger, A.N. Itakura, 2018. Young's modulus of plasma-polymerized allylamine films using micromechanical cantilever sensor and laser-based surface acoustic wave techniques, Plasma Processes Polym. 15, 1800083. https://doi.org/10.1002/ppap.201800083.

[47] L.M.H. Groenewoud, G.H.M. Engbers, J.G.A. Terlingen, H. Wormeester, J. Feijen, Pulsed plasma polymerization of thiophene, Langmuir 16 (2000) 6278–6286. https://doi.org/10.1021/la000111b.

[48] A.A. Puranik, L.N. Rodrigues, J. Chau, L. Li, K.K. Sirkar, 2019. Porous hydrophobic–hydrophilic composite membranes for direct contact membrane distillation, J. Membr. Sci. 591, 117225. https://doi.org/10.1016/j.memsci.2019.117225.

[49] W. Chen, A.Y. Fadeev, M.C. Hsieh, D. Öner, J. Youngblood, T.J. McCarthy, Ultrahydrophobic and ultralyophobic surfaces: Some comments and examples, Langmuir 15(10) (1999) 3395–3399. https://doi.org/10.1021/la990074s.

[50] M.T. Weise, S.C. Selbrede, L.J. Arias, D. Carl, Characterization of fluorinated tetra ethyl ortho silicate oxide films deposited in a low pressure plasma enhanced chemical vapor deposition reactor, J. Vac. Sci. Technol., A 15 (1997) 1399–1402. https://doi.org/10.1116/1.580549.

[51] M.A. Kudryashov, A.A. Logunov, L.A. Mochalov, Direct one-stage plasma-chemical synthesis of chalcogenide films doped with ytterbium, J. Phys.: Conf. Ser. 1967 (2021). https://doi.org/10.1088/1742-6596/1967/1/012005.

[52] W. Chen, S. Chen, T. Liang, Q. Zhang, Z. Fan, H. Yin, K.-W. Huang, X. Zhang, Z. Lai, P. Sheng, High-flux water desalination with interfacial salt sieving effect in nanoporous carbon composite membranes, Nat. Nanotechnol. 13 (2018) 345–350. https://doi.org/10.1038/s41565-018-0067-5.

[53] J. Ortiz-Medina, H. Kitano, A. Morelos-Gomez, Z. Wang, T. Araki, C.-S. Kang, T. Hayashi, K. Takeuchi, T. Kawaguchi, A. Tanioka, R. Cruz-Silva, M. Terrones, M. Endo, Nanostructured carbon-based membranes: nitrogen doping effects on reverse osmosis performance, NPG Asia Mater. 8 (2016) e258–e258. https://doi.org/10.1038/am.2016.27.

[54] S. Samitsu, H.T. Miyazaki, H. Segawa, Transmitting and scattering colors of porous particles of poly(vinyl chloride) based on Christiansen effect, Polymer 147 (2018) 237–246. https://doi.org/10.1016/j.polymer.2018.06.003.

[55] P. Kirkegaard, M. Eldrup, POSITRONFIT: A versatile program for analysing positron lifetime spectra, Comput. Phys. Commun. 3 (1972) 240–255. https://doi.org/10.1016/0010-4655(72)90070-7.

[56] P. Kirkegaard, M. Eldrup, POSITRONFIT extended: A new version of a program for analysing position lifetime spectra, Comput. Phys. Commun. 7 (1974) 401–409. https://doi.org/10.1016/0010-4655(74)90070-8.

[57] R.B. Gregory, Free-volume and pore size distributions determined by numerical Laplace inversion of positron annihilation lifetime data, J. Appl. Phys. 70 (1991) 4665 – 4670. https://doi.org/10.1063/1.349057.

[58] T. Takeuchi, M. Yamamoto, K. Nishimoto, Theoretical study on electron impact mass spectrometry. III. Ab initio MO study on the fragmentation of propylamine, J. Mass Spectrom. Soc. Jpn. 34 (1986) 267–278. https://doi.org/10.5702/massspec.34.267.

[59] W.Z. Collison, T.Q. Ni, M.S. Barnes, Studies of the low-pressure inductively-coupled plasma etching for a larger area wafer using plasma modeling and Langmuir probe, J. Vac. Sci. Technol, A 16 (1998) 100–107. https://doi.org/10.1116/1.580955.

[60] M.H. Khater, Effects of gas distribution on polysilicon etch rate uniformity for a low pressure, high density plasma, J. Vac. Sci. Technol, B 16 (1998) 490–495. https://doi.org/10.1116/1.589852.

[61] G. Merle, M. Wessling, K. Nijmeijer, Anion exchange membranes for alkaline fuel cells: A review, J. Membr. Sci. 377 (2011) 1–35. https://doi.org/10.1016/j.memsci.2011.04.043.

[62] S. Gottesfeld, D.R. Dekel, M. Page, C. Bae, Y. Yan, P. Zelenay, Y.S. Kim, Anion exchange membrane fuel cells: Current status and remaining challenges, J. Power Sources 375 (2018) 170–184. https://doi.org/10.1016/j.jpowsour.2017.08.010.

[63] A. Fahmy, T.A. Mohamed, J.F. Friedrich, XPS and IR studies of plasma polymers layer deposited from allylamine with addition of ammonia, Appl. Surf. Sci. 458 (2018) 1006–1017. https://doi.org/10.1016/j.apsusc.2018.07.160.

[64] T.R. Gengenbach, H.J. Griesser, Aging of 1,3-diaminopropane plasma-deposited polymer films: Mechanisms and reaction pathways, J. Polym. Sci., Part A: Polym. Chem. 37 (1999) 2191–2206. https://doi.org/10.1002/(sici)1099-0518(19990701)37:13<2191::Aid-pola34>3.0.Co;2-f.

[65] J. Robertson, Diamond-like amorphous carbon, Mater. Sci. Eng., R 37 (2002) 129–281. https://doi.org/10.1016/s0927-796x(02)00005-0.

[66] S.C. Ray, W.F. Pong, P. Papakonstantinou, Iron, nitrogen and silicon doped diamond like carbon (DLC) thin films: A comparative study, Thin Solid Films 610 (2016) 42–47. https://doi.org/10.1016/j.tsf.2016.04.048.

[67] A. K, A. Varade, N.R. K, S. Dhan, C. M, B. N, P. Krishna, Synthesis of high hardness IR optical coating using diamond-like carbon by PECVD at room temperature, Diamond Relat. Mater. 78 (2017) 39–43. https://doi.org/10.1016/j.diamond.2017.07.008.

[68] T. Schwarz-Selinger, A. von Keudell, W. Jacob, Plasma chemical vapor deposition of hydrocarbon films: The influence of hydrocarbon source gas on the film properties, J. Appl. Phys. 86 (1999) 3988–3996. https://doi.org/10.1063/1.371318.

[69] E.R. Nightingale Jr., Phenomenological theory of ion solvation: Effective radii of hydrated ions, J. Phys. Chem. 63 (2002) 1381–1387. https://doi.org/10.1021/j150579a011.

[70] H. Levine, L. Slade, Water as a plasticizer: physico-chemical aspects of low-moisture polymeric systems, Water Sci. Rev. 3 (1988) 79–185. https://doi.org/10.1017/cbo9780511552083.002.

[71] N. Ohtake, M. Hiratsuka, K. Kanda, H. Akasaka, M. Tsujioka, K. Hirakuri, A. Hirata, T. Ohana, H. Inaba, M. Kano, H. Saitoh, 2021. Properties and classification of diamond-like carbon films, Materials 14, 315. https://doi.org/10.3390/ma14020315.

[72] L.G. Jacobsohn, F.L. Freire Jr., Influence of the plasma pressure on the microstructure and on the optical and mechanical properties of amorphous carbon films deposited by direct current magnetron sputtering, J. Vac. Sci. Technol, A 17 (1999) 2841–2849. https://doi.org/10.1116/1.582022.

[73] S. Sourirajan, Characteristics of porous cellulose acetate membranes for separation of some organic substances in aqueous solution, Ind. Eng. Chem. Prod. Res. Dev. 4 (1965) 201–206. https://doi.org/10.1021/i360015a013

.[74] Y. Kiso, K. Muroshige, T. Oguchi, M. Hirose, T. Ohara, T. Shintani, Pore radius estimation based on organic solute molecular shape and effects of pressure on pore radius for a reverse osmosis membrane, J. Membr. Sci. 369 (2011) 290–298. https://doi.org/10.1016/j.memsci.2010.12.005.

[75] X. Qiao, T.-S. Chung, W.F. Guo, T. Matsuura, M.M. Teoh, Dehydration of isopropanol and its comparison with dehydration of butanol isomers from thermodynamic and molecular aspects, J. Membr. Sci. 252 (2005) 37–49. https://doi.org/10.1016/j.memsci.2004.11.014.

[76] W.F. Guo, T.-S. Chung, T. Matsuura, Pervaporation study on the dehydration of aqueous butanol solutions: A comparison of flux vs. permeance, separation factor vs. selectivity, J. Membr. Sci. 245 (2004) 199–210. https://doi.org/10.1016/j.memsci.2004.07.025.